Acta Pharmaceutica Sinica B 2024;14(6):2646–2656

Chinese Pharmaceutical Association
Institute of Materia Medica, Chinese Academy of Medical Sciences

Acta Pharmaceutica Sinica B

www.elsevier.com/locate/apsb
www.sciencedirect.com

ORIGINAL ARTICLE

Spirohypertones A and B as potent antipsoriatics: Tumor necrosis factor-α inhibitors with unprecedented chemical architectures

Yulin Duan[a,b,†], Weiguang Sun[a,†], Yongqi Li[a,†], Zhengyi Shi[a], Lanqin Li[a], Yeting Zhang[a], Kun Huang[a], Zhiping Zhang[a], Changxing Qi[a,*], Yonghui Zhang[a,*]

[a]*Hubei Key Laboratory of Natural Medicinal Chemistry and Resource Evaluation, Tongji Medical College, Huazhong University of Science and Technology, Wuhan 430030, China*
[b]*Department of Pharmacy, Wuhan No. 1 Hospital, Wuhan 430022, China*

Received 26 October 2023; received in revised form 29 December 2023; accepted 29 January 2024

KEY WORDS

Hypericum patulum;
Polycyclic polyprenylated acylphloroglucinols;
Tumor necrosis factor-α inhibitory activity;
Psoriasis

Abstract Tumor necrosis factor-α (TNF-α) is a promising target for inflammatory and autoimmune diseases. Spirohypertones A (**1**) and B (**2**), two unprecedented polycyclic polyprenylated acylphloroglucinols with highly rearranged skeletons, were isolated from *Hypericum patulum*. The structures of **1** and **2** were confirmed through comprehensive spectroscopic analysis, single-crystal X-ray diffraction and electronic circular dichroism calculations. Importantly, **2** showed remarkable TNF-α inhibitory activity, which could protect L929 cells from death induced by co-incubation with TNF-α and actinomycin D. It also demonstrated the ability to suppress the inflammatory response in HaCaT cells stimulated with TNF-α. Notably, in an imiquimod-induced psoriasis murine model, **2** restrained symptoms of epidermal hyperplasia associated with psoriasis, presenting anti-inflammatory and antiproliferative effects. This discovery positions **2** as a potent TNF-α inhibitor, providing a promising lead compound for developing an antipsoriatic agent.

*Corresponding authors.
E-mail addresses: qichangxing@hust.edu.cn (Changxing Qi), zhangyh@mails.tjmu.edu.cn (Yonghui Zhang).
[†]These authors made equal contributions to this work.

Peer review under the responsibility of Chinese Pharmaceutical Association and Institute of Materia Medica, Chinese Academy of Medical Sciences.

https://doi.org/10.1016/j.apsb.2024.02.002

1. Introduction

Psoriasis, a prevalent chronic inflammatory and autoimmune skin disease, affecting over 60 million people worldwide, lead to a substantial burden for society and individuals[1,2]. The pathogenesis of psoriasis remains unclear; however, various medical studies indicate the interleukin-17 (IL-17) and interleukin-23 (IL-23) as key drivers in psoriasis pathogenesis, while genetic susceptibility and environmental factors might trigger this disease [3,4]. Tumor necrosis factor α (TNF-α) is a proinflammatory cytokine produced by immune cells that possesses several biological effects and induces vascular adhesion molecules facilitating inflammatory cell influx, and amplifying the effects of other cytokines. TNF-α inhibitory effects could reduce the keratinocyte hyperproliferation and excessive inflammation that is instrumental in treating psoriasis[5,6]. Thus, TNF-α emerges as a promising therapeutic target to cure psoriasis[6].

TNF-α inhibitory monoclonal antibodies, such as adalimumab, infliximab, and etanercept, are widely used to treat autoimmune and inflammatory diseases, including psoriasis and rheumatoid arthritis[7]. However, these macromolecule agents face challenges such as low adaptability, high costs, and infectious susceptibility with prolonged use[8]. In contrast, small-molecule drugs offer industrialization feasibility, easy oral administration and cost-effectiveness[9]. Although small-molecule TNF-α inhibitors show a certain development prospect in new drugs research, there is still no small molecule drugs targeted inhibiting TNF-α in clinical usage up to now, so there is a struggle to find small molecule leading compounds that can treat diseases by inhibiting TNF-α[10].

Polycyclic polyprenylated acylphloroglucinols (PPAPs), a family of characteristic metabolites isolated from the genus *Hypericum*, originated from a "mixed" mevalonate/methylerythritol phosphate and polyketide biosynthetic pathway, followed by cyclization of the side chains and the degradation/reconstruction of the acylphloroglucinol core contributed to their complex structures[11,12]. Due to the various polycyclic systems, PPAPs often exhibit ample biological properties, such as antitumor, anti-HIV, antibacterial and immunosuppressive abilities[11-15]. As a part of our systematic exploration for intriguing PPAPs from *Hypericum* plants[16-19], the chemical constituents of *Hypericum patulum* were investigated, and two highly rearranged PPAPs, spirohypertones A (**1**) and B (**2**) (Fig. 1), were obtained and characterized. Remarkably, **1** shared an unparalleled 5/5/6/5 ring system, possibly derived from bicyclic polyprenylated acylphloroglucinol (BPAP) *via* the breakages of C-1/C-6 and C-1/C-2 linkages in the acylphloroglucinol core, along with the cyclization reactions between C-1/C-5 and C-3/C-20; **2** might be generated through the rupture of C-1/C-2 in the core and the ring formations of C-3/C-20. Importantly, **2** selectively inhibited TNF-α, promoting cell viability in an actinomycin D/TNF-α induced L929 cell death model and effectively blocking multiple inflammatory factors stimulated with TNF-α in HaCaT cells. Impressively, **2** alleviated symptoms of the epidermal hyperplasia associated with psoriasis by inhibiting the excessive proliferation of epidermal cells in an imiquimod-induced psoriasis murine model. Herein, the structural determination, plausible biogenetic pathways, and biological assay of **1** and **2** were reported.

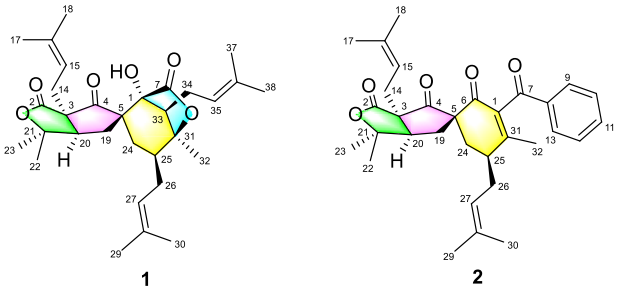

Figure 1 Structures of compounds **1** and **2**.

2. Results and discussion

2.1. Structural elucidation biosynthetic consideration for compounds *1* and *2*

Spirohyperton A (**1**) was initially obtained as a colorless oil, and its molecular formula, $C_{31}H_{44}O_6$, with 10 indices of hydrogen deficiency, was established by positive HRESIMS ion at HRMS (ESI) data (*m/z*: $[M + Na]^+$ Calcd. 535.3030; Found 535.3022). The IR spectrum of **1** displayed strong absorption bands corresponding to hydroxyl (3466 cm^{-1}), γ-lactone carbonyl (1775 cm^{-1}), and ketone carbonyl (1731 cm^{-1}) groups. The characteristic signals of nine methyls, three olefinic protons, and one exchangeable proton were found based on its ^1H NMR spectrum. In its ^{13}C and DEPT NMR spectra, clear signals of 31 carbons were observed, classified as nine methyls, five methylenes, six methines (three olefinic), and eleven nonprotonated carbons (three olefinic ones, two ester carbonyls, one ketone carbonyl, and three oxygenated ones). From the above characteristic data and the reports of diverse PPAPs obtained from the genus *Hypericum*, **1** was likely to be a PPAP derivative featuring a tetracyclic skeleton[11,16-20] (Fig. 1).

The planar structure of **1** was established by interpreting its NMR spectroscopic data (Fig. 2). The HMBC correlations from 1-OH to C-1, C-5 and C-33; from H_2-24 to C-1, C-5 and C-31; and from H_3-32 to C-25, C-31 and C-33; from H-20 to C-3 and C-4; from H_2-19 to C-1, C-4, C-5 and C-24, accompanied by the $^1H-^1H$ COSY cross-peaks of H_2-24/H-25/H_2-26/H-27 and H_2-19/H-20, confirmed the fusion of rings A and B to construct the unusual spiro[4.5]decane core. Furthermore, one ester carbonyl (C-2) was connected to C-3, defined by the key HMBC correlations from H_2-14/H-20 to C-2, and another ester carbonyl (C-7) was linked at C-1 supported by the HMBC correlation from 1-OH to C-7. In addition, the HMBC interactions from H_2-14 to C-3 and C-4; H_3-17 to C-15 and C-18; from H_2-24 to C-26; from H_3-29 to C-27 and C-30; and from H_3-37 to C-35 and C-38, with the aid of the $^1H-^1H$ COSY cross-peaks of H_2-14/H-15, H_2-24/H-25/H_2-26/H-27 and H-33/H_2-34/H-35, suggested that three isoprenyl groups were positioned at C-3, C-25 and C-33, respectively. Moreover, the HMBC correlations from H_3-22 to C-20, C-21 and C-23 suggested that an *iso*-propyl-liked moiety was attached at C-20. Thus, there were four "loose ends" in **1**, as shown in Fig. 2.

According to its HRESIMS data, **1** possessed ten indices of hydrogen deficiency, while the presence of rings A and B, three carbonyl and six olefinic groups accounted for eight degrees of unsaturation, indicating the existence of two lactone rings in **1**. A comprehensive analysis suggested two plausible planar structures for **1**: the first assumption was two additional lactone rings located between C-2 and C-21, and between C-7 and C-31 (possible structure **1a**, Supporting Information Fig. S1), while the second speculation was two lactone rings located between C-2 and C-31,

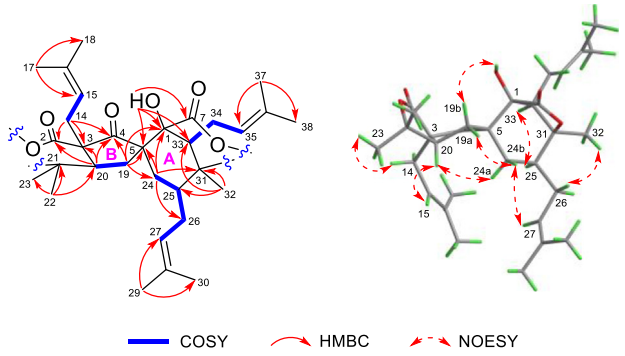

Figure 2 Key 2D NMR correlations of **1**.

and between C-7 and C-21 (possible structure **1b**, Fig. S1). Considering the chemical shift of C-21 located at a field region at δ_C 84.7 (Supporting Information Table S1), and the characteristic absorption band at 1775 cm^{-1} in IR spectrum, resembling the known compounds possessing the similar five-membered lactone ring, we speculated that **1a** should be more reasonable[18,20-22]. Therefore, the planar construction of **1**, possessing a highly rearranged carbon architecture, was finally defined.

A NOESY test was conducted to reveal the relative configuration of **1** (Fig. 2), in which the cross-peaks of 1-OH/H-19b, H-19a/H-24b, H-20/H-24a, H-20/H-15, and H_2-14/H_3-23 indicated that the C-1−C-5 bond was located at the axial to the ring B, assigned as β-orientation. Consequently, H-20 and the prenyl group at C-3 were situated on the opposite side to the C-1−C-5 bond, defined as α-orientation. Then, the NOESY interactions of H-25/H-33 and H_2-26/H_3-32, along with a large coupling constant ($^3J_{H\text{-}24b,H\text{-}25}$ = 11.2 Hz), and the conformation of the bicyclo [3.2.1]nonane system, demonstrated that 1-OH, H-25, H_3-32, and H-33 were α-orientated. Thus, the relative configuration of **1** was confirmed.

The highly rearranged architecture of **1** and its multiplex chiral centers stimulated us to attempt its identification by crystallography. After repeated attempts, a suitable crystal of **1** was obtained from a mixed solution system (methanol:tetrahydrofuran: H_2O = 8:1:1), which subsequently underwent a single-crystal X-ray diffraction test with Cu Kα radiation, supporting our conclusion regarding its absolute structure based on a Flack parameter of 0.01 (5) (CCDC 2123523) (Fig. 3).

Spirohyperton B (**2**) was obtained as colorless crystals. Its molecular formula, $C_{32}H_{38}O_5$ (14 degrees of unsaturation), was adequately identified by HRMS (ESI) data (*m/z*: $[M + Na]^+$ Calcd. 525.2611; Found 525.2619) and ^{13}C NMR data. The ^1H NMR spectrum showed typical signals for seven singlet methyl groups, two olefinic protons, and one monosubstituted benzene group. There were 32 carbons presented in its ^{13}C NMR spectrum, consistent with its molecular formula, resolved into seven methyls, four methylenes, nine methines (including five aromatic and two olefinic carbons), and twelve nonprotonated carbons (four carbonyls, five olefinic ones, and one oxygenated carbon) by analysis of the DEPT and HSQC data. From the accumulative analysis, **2** should be a PPAP derivative possessing a tricyclic ring system.

The planar structural elucidation of **2** was fully represented by analyzing its 2D NMR spectra (Fig. 4). The observed HMBC interactions from H_2-24 to C-5, C-6 and C-31; from H_3-32 to C-1, C-25 and C-31; and from H-9 to C-7, combined with the $^1H-^1H$ COSY cross-peaks of H_2-24/H-25/H_2-26/H-27 and H-9/H-10/H-11/H-12/H-13 established the connectivity of the six-membered ring A. Moreover, the HMBC correlations from H_2-14 to C-2, C-3 and C-4; from H_2-19 to C-4, C-5, C-6 and C-24; and from H-20 to C-2 and C-3, aided by the $^1H-^1H$ COSY cross-peak of H_2-19/H-20, firmly constructed the five-membered ring B linked to ring A with a spiro junction at C-5. In addition, the obvious downfield shift appeared at C-21 (δ_C 86.5), and the remaining degree of unsaturation in **2** suggested the linkage of C-21 and C-2 *via* an oxygen atom, forming the γ-lactone ring C. Hence, the gross planar structure of **2** with an extraordinary 5/5/6 ring system was confirmed.

The relative configuration of **2** was defined by fully expounding the NOESY data (Fig. 4). In the NOESY spectrum, the cross-peaks of H_2-14/H_3-23, H-15/H-20, H-20/H-24a and H_3-18/H-25 unquestionably proved that the relative configurations of C-3, C-5, C-20 and C-25 in **2** were identical to those of **1**, assigned as 3*R**,5*R**,20*R**,25*S**. Additionally, the isolate **2** possessed a new 5/5/6 skeleton, and its formation involved a series of complicated reactions, differing from those of **1**. To address its absolute configuration, a suitable crystal was obtained after several attempts, allowing us to arbitrarily defined it as 3*R*,5*R*,20*R*,25*S* (Fig. 3). Furthermore, electronic circular dichroism (ECD) calculations using TDDFT method at PBE0/def2-TZVP level in methanol were conducted, and the experimental

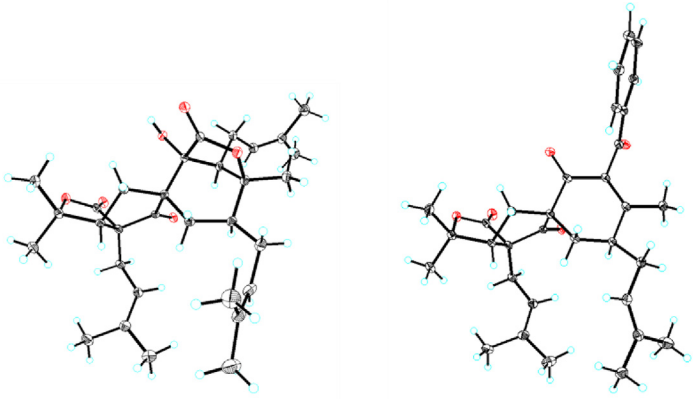

Figure 3 The X-ray structures of **1** and **2**.

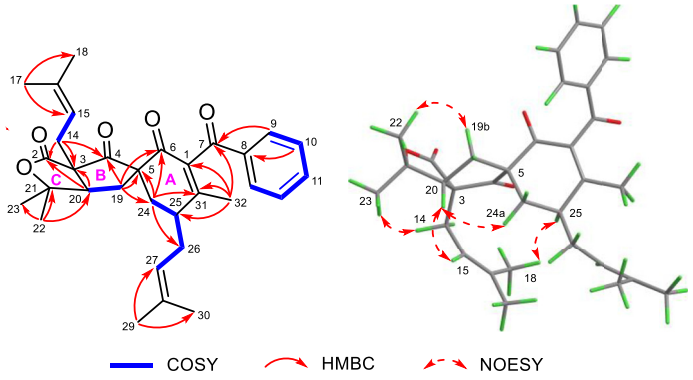

Figure 4 Key 2D NMR correlations of compound **2**.

ECD curve was fully consistent with the calculated one, further validating its absolute configuration (Fig. 5).

Spirohypertones A (**1**) and B (**2**) were highly functionalized and rearranged PPAPs with unparalleled carbon skeletons, diverging from the known PPAPs[11,18,22-27]. Thus, a plausible biogenetic pathway was proposed. As shown in Scheme 1, starting from a common precursor, monocyclic polyprenylated acylphloroglucinol (MPAP, **i**), the addition of dimethylallyl diphosphate (DMAPP), followed by oxidation, cyclization and keto-enol tautomerism, could produce the crucial intermediate [4.3.1]-type BPAP (**ii**)[11], which then underwent retro-Claisen by cleaving the C-1−C-6 bond of acylphloroglucinol core, followed by decarboxylation, intramolecular cyclization and keto-enol tautomerism to produce **iii**[28-30]. The subsequent cleavage of the C-1−C-2 bond *via* retro-Claisen and oxidation in **iii** might further decorate **iv**, followed by intramolecular cyclization between C-3/C-20, yielding key intermediate **v**. Finally, Baeyer-Villiger oxidation in **v**, and further hydrolysis and esterification reactions could generate **1** bearing an unexpected 5/5/6/5 tetracyclic ring system. In addition, the intermediate **i** could undergo oxidation and intramolecular cyclization reactions to construct the critical intermediate [3.3.1]-type BPAP (**vi**)[11]. Retro-Claisen and oxidation reactions in **vi**, followed by intramolecular cyclization and esterification could further build the novel PPAP, possessing a unique 5/5/6 tricyclic ring system.

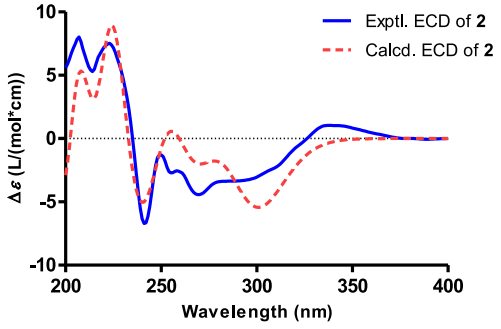

Figure 5 Experimental and calculated ECD spectra for compound **2**.

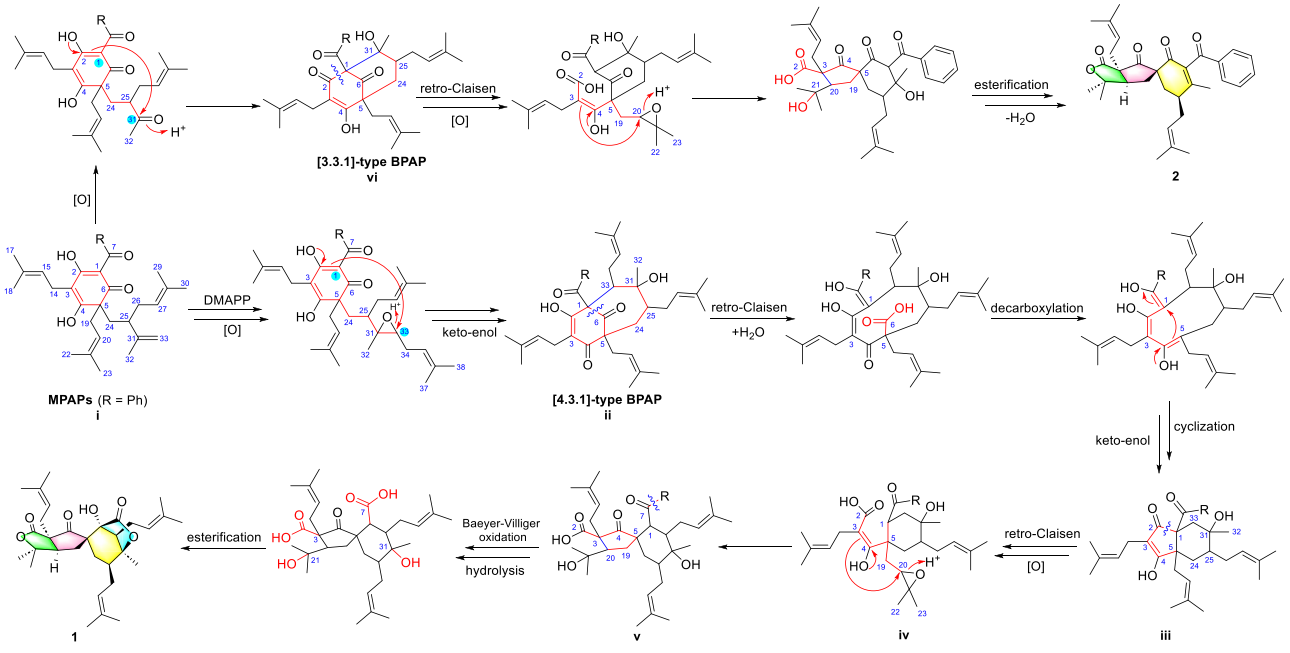

Scheme 1 Plausible biosynthetic pathways of **1** and **2**.

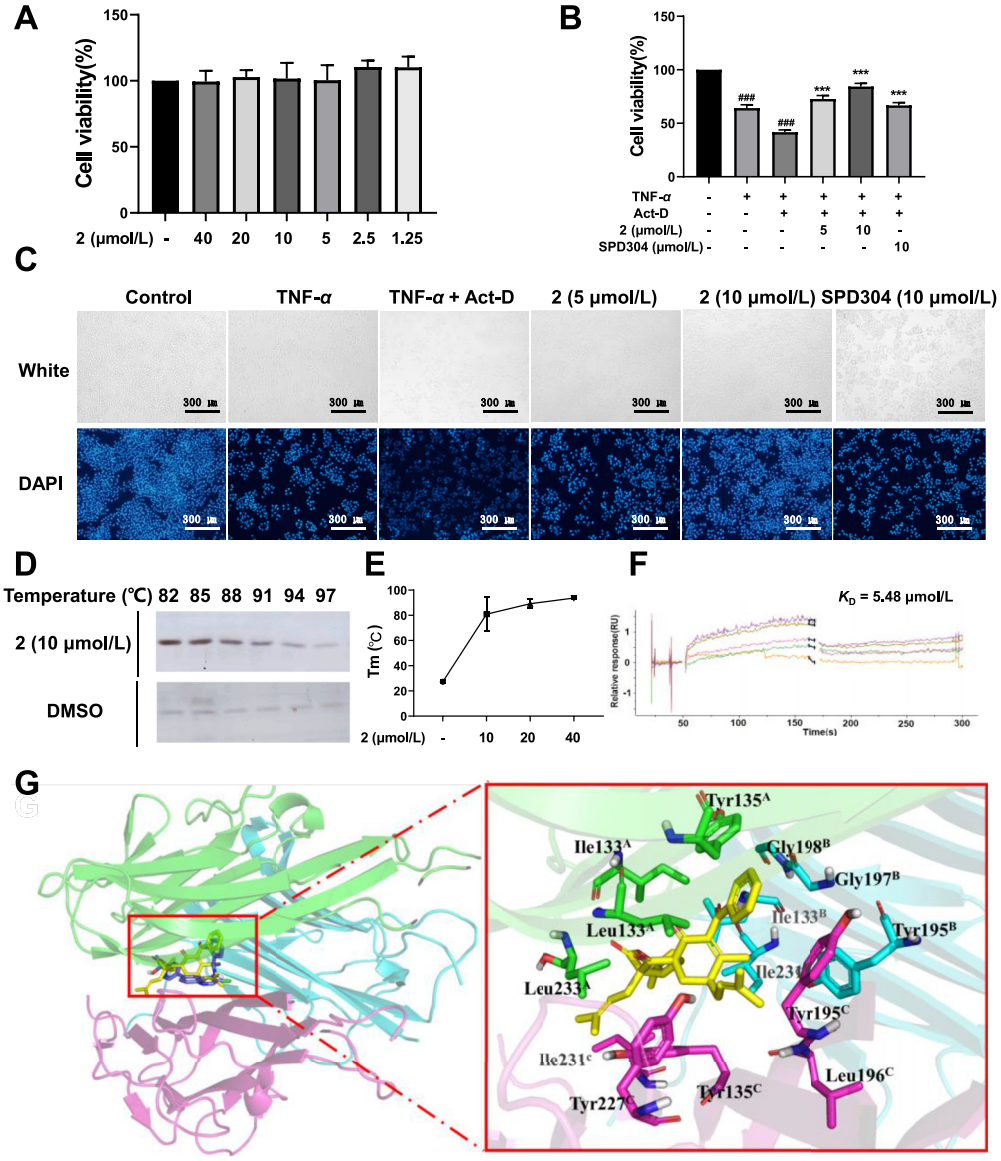

Figure 6 The targeted inhibitory activity of **2** against TNF-α. (A) Cytotoxicity of **2** on L929 cells. (B−C) Cell viability, morphology and DAPI staining analysis after treatment with or without TNF-α, actinomycin D, and **2**. Concentration-dependent inhibition of TNF-α by **2**. (D−E) CETSA and TSA assay to detect the thermal stability of purified TNF-α protein. (F) SPR assay to measure the binding affinity between **2** and TNF-α. (G) Overall structure with the surface of TNF-α and **2** (Chain A, B and C in green, blue and pink, respectively, and **2** shown in yellow). Data are presented as mean ± SD. $^{###}P < 0.001$ compared with control, $^{***}P < 0.001$, compared with model. Scale bar: 300 μm.

2.2. *Targeted inhibitory activity of compound 2 against TNF-α*

The cytokine TNF-α substantially contributes to the pathogenesis of psoriasis, and it harbors a potent target for psoriasis treatment[1,6]. Herein, a TNF-α induced L929 cell death model was developed to evaluate the TNF-α inhibitory capacity of **1** and **2**[31-34]. As shown in Fig. 6A and B and Supporting Information Fig. S27, **1** and **2** had no evident cytotoxicity even at 40 μmol/L, and **2** could more effectively protect L929 cells from death induced by co-incubation with TNF-α and actinomycin D in a concentration-dependent manner. The presence of morphology and DAPI staining analysis also suggested the potential of **2** for targeted TNF-α inhibition, which was even better than that of positive control, SPD304 (Fig. 6C). To further confirm that **2** can directly target TNF-α, cellular thermal shift assay (CETSA), thermal shift assay (TSA), and surface plasmon resonance (SPR) assay were used[35]. The results showed that **2** improved the cellular thermal stability of TNF-α, increasing the tolerable temperature from 86 to 100 °C (Fig. 6D and E). The SPR assay showed that **2** could directly bind to TNF-α with a value of 5.48 μmol/L, indicating an effective binding affinity that was similar to that of the positive control, SPD304 (Fig. 6F, Supporting Information Fig. S28).

To further investigate their structure−activity relationship and modes of action, the binding modes and energies of **2** with TNF-α were obtained by molecular docking. As shown in Fig. 6G, the

binding pocket of the TNF-α tripolymer was relatively sharp and fusiform; thus, **2** could fully occupy the binding site of the crystallographic ligand SPD304 to prevent the assemble of a biologically active trimer complex. Hydrophobic interactions were observed between **2** and key residues, including Ile133, Leu233, Tyr135 and Tyr227, from TNF-α monomers. In particular, the benzyl group in **2** exhibited strong π−π interactions with the $Tyr195^{C}$ residue, which played an important role in stabilizing the ligand binding.

2.3. Compound 2 blocks inflammatory factors in TNF-α stimulated HaCaT cells

The effects of **2** on key signaling pathways related to psoriasis in HaCaT cells were examined. **2** exhibited significant inhibition of TNF-α induced inflammatory factors, including IL-23, CXCL1 and S100A9 with minimal toxicity (Fig. 7A, Supporting Information Fig. S29). Furthermore, the results of immunofluorescence illustrated the ability of **2** to inhibit the nuclear translocation of NF-κB p65 induced by TNF-α (Fig. 7B). Taken together, these results demonstrated that **2** could effectively block multiple inflammatory factors *via* targeted TNF-α inhibition.

2.4. Compound 2 alleviates the epidermal hyperplasia symptoms of IMQ-induced psoriasis in mice

To assess the *in vivo* effects of **2** on psoriasis, the psoriasis mice model induced by IMQ was established. The IMQ group showed significant thickening and erythema, and continuously increasing clinical severity score (CSS) (Fig. 8A and B), while **2** remodeled psoriasis-like dermatitis in a dose-dependent manner, as characterized by the reduced severity of skin erythema and scales, skin thickness, and CSS. The HE staining results showed that the skin lesions in the IMQ group had similar histologic features with significant epidermal hyperplasia, scaling, and an intense inflammatory response. However, this condition could be improved using **2** and the positive drug tapinarof treatment (Fig. 8C). As an important cytokine in the pathogenesis of psoriasis, IL-17 can act synergistically with TNF-α to further amplify inflammatory signals, while Ki67 is a marker of cell proliferation, reflecting the degree of active cell proliferation[1]. According to the immunohistochemical results (Fig. 8C), Ki67 was up-regulated and IL-17 expression appeared discontinuous in the upper layer of the skin from the IMQ group. In contrast, the **2**-treated group showed down-regulation of Ki67 and restoration of the continuous IL-17 expression, suggesting that **2** could alleviate the epidermal hyperplasia symptoms of psoriasis by inhibiting excessive epidermal cell proliferation.

3. Conclusions

In conclusion, spirohypertones A (**1**) and B (**2**), two new PPAPs with highly rearranged skeletons, were isolated from *H. patulum*. Compound **1** possessed an unparalleled 5/5/6/5 tetracyclic system, that should be formed from [4.3.1]-type-BPAP by the disconnections of C-1/C-6 and C-1/C-2 linkages in the

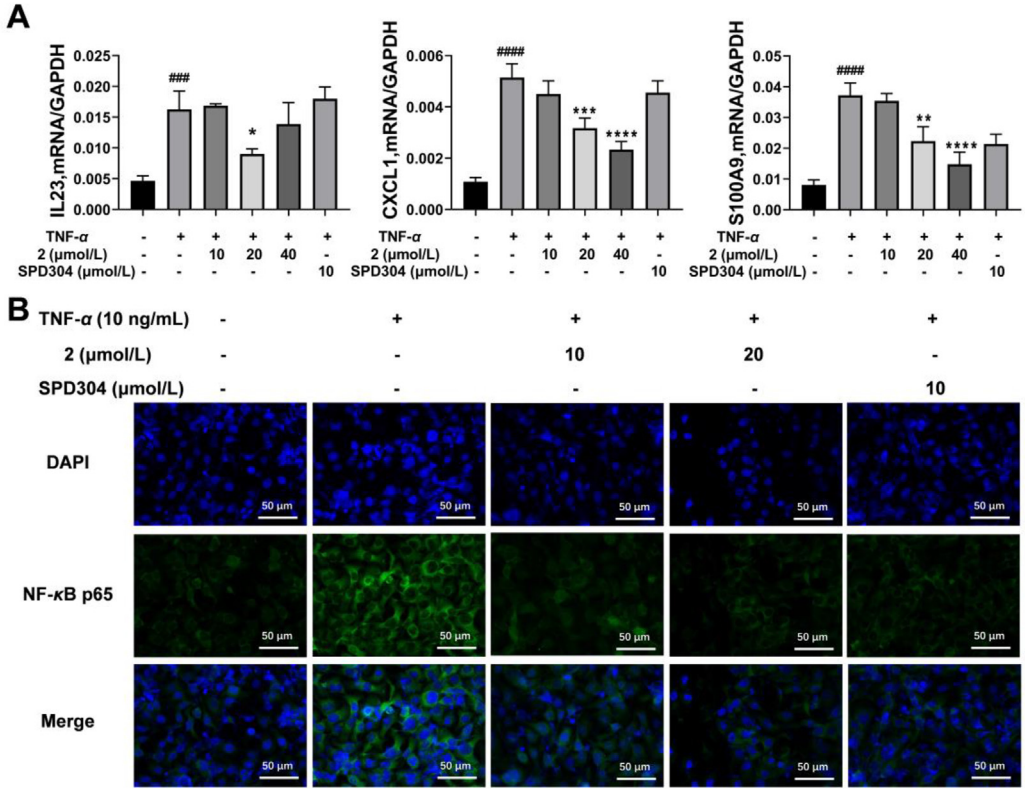

Figure 7 Inhibition of TNF-α induced inflammatory response in HaCaT cell by **2**. (A) The mRNA expression levels of IL-23, CXCL1, and S100A9, were measured using RT-qPCR. (B) **2** inhibited TNF-α induced NF-κB p65 phosphorylation and nuclear translocation. Data are presented as mean ± SD. $^{###}P < 0.001$ compared with control, $^{*}P < 0.05$, $^{**}P < 0.01$, $^{***}P < 0.001$, $^{****}P < 0.0001$ compared with model. Scale bar: 50 μm.

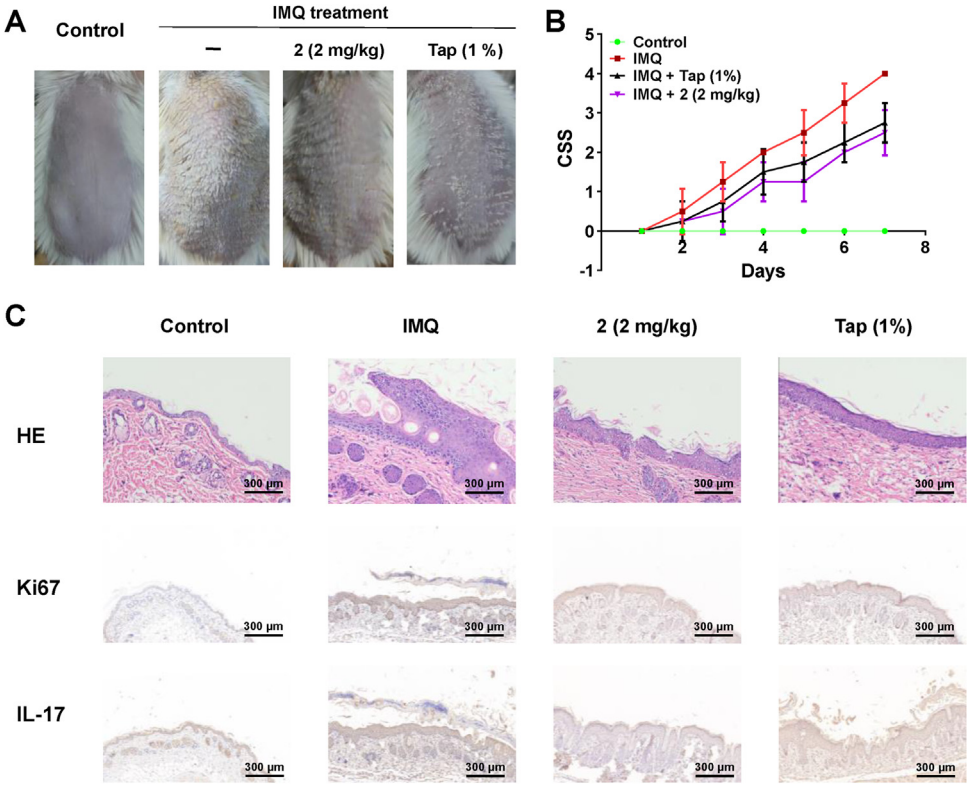

Figure 8 The pharmacodynamic effects of **2** on IMQ-induced psoriasis in mice. (A) Observation of skin lesions in control group, **2**-treated group, and tapinarof treatment group after 7 consecutive days treatment. (B) Quantification of CSS in mice from each group. (C) Manifestation and histological features of skin lesions in each group. Scale bar: 300 μm.

acylphloroglucinol core, along with multistep realignments of C-1/C-5 and C-3/C-20; **2** equipped with a unique 5/5/6 tricyclic ring system that might be from [3.3.1]-type-BPAP by the interruption of C-1/C-2 in the core and the rearrangements of C-3/C-20. Importantly, **2** could increase cell viability in L929 cells stimulated by TNF-α and actinomycin D, effectively blocking inflammatory factors in TNF-α stimulated HaCaT cells, as a potential TNF-α inhibitor. Furthermore, *in vivo* experiments indicated that **2** could relieve symptoms of epidermal hyperplasia associated with psoriasis by inhibiting excessive epidermal cell proliferation. These findings might provide a potential candidate as a TNF-α inhibitor to treat psoriasis for further research on pharmacology and synthesis.

4. Experimental

4.1. *General experimental procedures*

NMR data were acquired on Bruker AM-400 spectrometers with TMS as the internal standard. HRMS (ESI-TOF) data were obtained by using a Bruker micOTOF II and SolariX 7.0 spectrometer (Bruker, Karlsruhe, Germany). X-ray crystallographic data were collected on an XtaLAB PRO MM007HF (Rigaku, Japan) instrument with Cu Kα radiation. The melting point of the crystal was measured on an X-5 microscopic melting point apparatus (Beijing Tech, China). ECD spectra were collected on a JASCO-810 spectrometer (JASCO, Tokyo, Japan). IR spectra were acquired by using a Bruker Vertex 70 FT-IR spectrophotometer (Bruker, Karlsruhe, Germany). Optical rotations were acquired by using a PerkinElmer 341 polarimeter (PerkinElmer Inc., Fremont, CA, USA). UV spectra were obtained on a Lambda 35 instrument (PerkinElmer Inc., Fremont, CA, USA). Semi-preparative HPLC was conducted on an Agilent 1200 system or a Dionex HPLC system with a reversed-phase (RP) C_{18} column (5 μm, 10 mm × 250 mm, Welch Ultimate XB-C_{18}) for separation and purification. Column chromatography (CC) including silica gel (80−120 and 100−200 mesh; Qingdao Marine Chemical Inc., China), Sephadex LH-20 (40−70 μm, Amersham Pharmacia Biotech AB, Uppsala, Sweden), and ODS (50 μm, YMC Co., Ltd., Japan) was used.

4.2. *Plant material*

The dried leaves of *H. patulum* were collected from the Enshi Tujia and Miao Autonomous Prefecture, in Hubei Province, People's Republic of China, in August 2018. The plants were identified by Prof. ChangGong Zhang of Huazhong University of Science and Technology (HUST). A voucher sample (No. HP20180824) was deposited in the herbarium of Tongji Medical College of HUST.

4.3. *Extraction, isolation and spectroscopic data*

The isolation was guided by the Surface Plasmon Resonance-based Active Molecules Recognition Strategy (SPR-AMRS) referring the reported paper[35]. Dried leaves of *H. patulum* (35.0 kg) were ground and extracted with 95% EtOH (25 L) five times at room temperature to obtain a crude extract. The crude extract was then suspended in

water and partitioned with CH_2Cl_2 to obtain the CH_2Cl_2 fraction (2.5 kg). This fraction was chromatographed on a silica gel CC (80−120 mesh) and eluted with a stepwise gradient of petroleum ether−ethyl acetate (50:1−0:1) to generate fractions (A−G). Fr. D (105 g) was separated into six fractions (D1−D6) loaded on a silica gel column with an eluent of petroleum ether/ethyl acetate (40:1 to 1:1). Fr. D4 (10 g) was loaded on an MCI column (MeOH−H_2O, 90:10 to 100:0) to remove pigments, followed by a RP-C_{18} column (MeOH−H_2O, 40:60 to 100:0) to afford nine subfractions, D4a−D4i. Fr. D4b (1.0 g) was subjected to Sephadex LH-20 CC (MeOH−CH_2Cl_2, 1:1, *v*/*v*) to obtained three subfractions, D4b1−D4b3. Fr. D4b2 (280 mg) was purified by RP HPLC repeatedly to obtain **2** (3.3 mg, t_R = 10.5 min, CH_3OH−H_2O, 93%). Fr. D4c (900 mg) was divided into three subfractions, D4c1−D4c3, by using Sephadex LH-20 CC (MeOH−CH_2Cl_2, 1:1, *v*/*v*). Then, Fr. D4c2 (300 mg) was purified by semi-preparative HPLC to yield **1** (3.8 mg, t_R = 25.5 min, CH_3OH−H_2O, 90%).

Spirohypertone A (**1**): colorless block crystals; mp 138.2−138.9 °C; $[\alpha]_D^{29}$−10.2 (c 0.2, CH_3OH); UV (CH_3OH) λ_{max} (log ε) = 200 (3.37) nm (Supporting Information Fig. S9); IR (KBr) ν_{max} 3466, 2973, 2920, 2857, 1775, 1731, 1449, 1383, 1263, 1166, 1129, 1091, 1027 and 955 cm^{-1} (Supporting Information Fig. S10); ECD (CH_3OH) λ_{max} ($\Delta\varepsilon$) 205 (+3.38), 223 (−4.95), 253 (+0.23) nm. ^1H and ^{13}C NMR data, see Supporting Information Figs. S2−S7 and Table S1; positive HRESIMS: *m*/*z* 535.3022 $[M + Na]^+$ (calcd. for $C_{23}H_{34}O_7Na^+$, 535.3030) (Supporting Information Fig. S8).

Spirohypertone B (**2**): colorless block crystals; mp 139.4−143.8 °C; $[\alpha]_D^{29}$ −15.2 (c 0.1, CH_3OH); UV (CH_3OH) λ_{max} (log ε) = 201 (4.52) nm (Supporting Information Fig. S24); IR (KBr) ν_{max} 2980, 2919, 2856, 1776, 1729, 1679, 1656, 1619, 1597, 1449, 1378, 1324, 1264, 1168, 1131, 954 and 691 cm^{-1} (Supporting Information Fig. S25); ECD (CH_3OH) λ_{max} ($\Delta\varepsilon$) 204 (+8.12), 241 (−7.14), 249 (−0.41), 269 (−4.45), 337 (+1.05) nm. ^1H and ^{13}C NMR data, see Supporting Information Figs. S11−S22 and Table S1); positive HRESIMS: *m*/*z* 525.2619 $[M + Na]^+$ (calcd. for $C_{23}H_{34}O_7Na^+$, 525.2611) (Supporting Information Fig. S23).

4.4. X-ray crystallographic analysis

A suitable block crystal of **1** was obtained in a methanol/tetrahydrofuran/H_2O solvent system (8:1:1) at 4 °C, and a block crystal of **2** was obtained in methanol at 4 °C, which were analyzed using a Bruker APEX DUO diffractometer. Cell refinement and data reduction were performed with Bruker SAINT. Crystallographic data (excluding structure factor tables) for the reported structures have been submitted to the Cambridge Crystallographic Data Center (CCDC) as a supplementary publication (CCDC No. for **1**: 2123523; for **2**: 2302409).

Crystallographic data of **1**: $C_{31}H_{44}O_6$, M = 512.66, a = 12.91230 (10) Å, b = 15.16440 (10) Å, c = 29.3480 (2) Å, α = 90°, β = 90°, γ = 90°, V = 5746.55 (7) $Å^3$, T = 293 (2) K, space group $P212121$, Z = 8, μ(CuKα) = 0.646 mm^{-1}, 65,729 reflections measured, 11496 independent reflections (R_{int} = 0.0458). The final R_1 values were 0.0367 ($I > 2\sigma(I)$). The final $wR(F^2)$ values were 0.0902 ($I > 2\sigma(I)$). The final R_1 values were 0.0392 (all data). The final $wR(F^2)$ values were 0.0920 (all data). The goodness of fit on F^2 was 1.022. Flack parameter = 0.01 (5).

Crystallographic data of **2**: $C_{32}H_{38}O_5$, M = 502.62, a = 6.42740 (10) Å, b = 19.7359 (3) Å, c = 21.8762 (3) Å, α = 90°, β = 90°, γ = 90°, V = 2775.01 (7) $Å^3$, T = 293 (2) K, space group $P212121$, Z = 4, μ(CuKα) = 0.637 mm^{-1}, 30,939 reflections measured, 5572 independent reflections (R_{int} = 0.0677). The final R_1 values were 0.0379 ($I > 2\sigma(I)$). The final $wR(F^2)$ values were 0.0961 ($I > 2\sigma(I)$). The final R_1 values were 0.0416 (all data). The final $wR(F^2)$ values were 0.0983 (all data). The goodness of fit on F^2 was 1.057. Flack parameter = 0.00 (9).

4.5. Computational methods

The details of ECD calculations for **2** were included in the Supporting Information (Supporting Information Fig. S26, Tables S2 and S3).

4.6. Cell viability analysis

L929 cells were maintained in minimum essential medium (MEM) (supplemented with 15% heat-inactivated FBS and 100 units/mL penicillin/streptomycin) at 37 °C in a humidified atmosphere of 5% carbon dioxide (CO_2). L929 cells were seeded at a density of 1 × 10^4 cells/mL in 96-well plates in 100 μL volume. After preincubation for 24 h in the humidified incubator at 37 °C and 5% CO_2, the cells were treated with compounds ranging from 40 to 1.25 μmol/L for 24 h. Absorbance was measured at 450 nm using a microplate reader to determine the cell viability as described in CCK-8 instructions.

4.7. Expression and purification of recombinant TNF-α protein

The recombinant pET-28a plasmid encoding TNF-α was transformed into *E. coli* BL21 (DE3) cells (Invitrogen) and cultured in Luria-Bertani medium (LB) at 37 °C. Protein expression was induced with 0.4 mmol/L IPTG at 180 rpm and 20 °C for 20 h. The details of TNF-α protein purification were previously reported with some modifications. The bacterial precipitate, obtained through centrifugation of the bacterial sap, was suspended in Lysis Buffer (50 mL), and bacterial cells were ultrasonicated 3−5 times, at 5 min intervals between two crushes. Soluble C-terminally hexahistidine-tagged TNF-α was bound to Ni-agarose affinity resin (Qiagen), washed with a buffer containing 20 mmol/L Tris, pH 8.5, 200 mmol/L NaCl, and 10 mmol/L imidazole, and eluted with a buffer containing 20 mmol/L Tris, pH 8.5, 250 mmol/L NaCl, and 150 mmol/L imidazole. 10 mL of TNF-α and ULP1 enzyme (mass ratio = 1:10) were placed on a 4 °C rotary shaker, and enzyme digestion was carried out overnight. The mixture was added to an empty gravity column, and the flow-through solution was collected. Purified TNF-α protein was quick-frozen and stored at −80 °C for subsequent experiments.

4.8. TNF-α-induced L929 cell death inhibition assay

L929 cells were seeded at a density of 1 × 10^4 cells/mL in 96-well plates in 100 μL volume. After preincubation for 24 h, the cells were treated with 5 and 10 μmol/L of **2** for another 24 h, followed by exposure to TNF-α (10 ng/mL) and actinomycin D (1 μg/mL) for another 24 h. Absorbance was measured at 450 nm using the microplate reader to determine the cell viability, as described in the CCK-8 instructions. Cell viability ratio (%) = $OD_{450\ treated}$/$OD_{450\ blank}$ × 100. SPD304 was selected as the positive control. Meanwhile, DAPI staining was performed by fixing cells with paraformaldehyde for 30 min, adding the appropriate amount of

DAPI staining solution for 5 min at room temperature, washing with PBS, and observing under a fluorescence microscope.

4.9. Cellular thermal shift assay

The purified TNF-α protein was incubated with **2** at 4 °C for 3 h. Proteins were incubated at different temperatures for 10 min, and 5 × loading buffer was added. 4 ng total proteins were used for each blot. The samples were separated by SDS-PAGE. The gel was fixed with fixative (ethanol:acetic acid:double-distilled water = 5:1:4) for 20 min, followed by sequential washes with 30% ethanol and double-distilled water for 10 min each. A sensitizing solution was added for 2 min and washed with water for 1 min twice. The gel was then incubated with the silver solution for 10 min, rinsed with water, and added to the color development solution, which was developed until a band, appeared and then terminated with the silver staining termination solution.

4.10. Thermal shift assay

The purified TNF-α protein was added into **2** to incubate at room temperature for 30 min. A fluorescent dye was added to the mixture, and the reaction was carried out in ABI Quant Studio 5. The mixture was heated to 95 °C at 0.075 °C/s and the dissolution curve was observed.

4.11. Surface plasmon resonance

Purified TNF-α proteins were pre-enriched for ligands on the Biacore 1K Molecular Interaction Analysis System to determine the optimal coupling concentration and pH conditions. The ligand was immobilized onto the CM5 chip using the amino coupling method to enrich the protein on the chip, and then the affinity between the protein and **2** was examined through the LMW multi-cycle kinetics/affinity program in the Biacore 1K Control Software.

4.12. Virtual docking

The crystal structure of TNF-α protein (PDB code: 7JRA) complexed with SPD304 was used in the docking study. Before docking studies, all water molecules in protein were removed, and all hydrogen atoms were added to the proteins by using Discovery Studio 3.5 with a CHARMm force field. The 3D structures of the compounds were sketched using ChemDraw 3D software. The binding site was defined as a sphere containing residues that stay within 10 Å of the ligand, which was large enough to cover the native ligand binding region at the active site. CDOCKER (DS3.5) and AutoDock Vina (version 1.1.2) were selected and applied for virtual screening. Scoring functions and docking parameters were optimized in advance by docking the native ligand complexed with TNF-α protein back to the active site of their receptor.

4.13. HaCaT cells viability analysis

HaCaT cells were maintained in MEM (supplemented with 15% heat-inactivated FBS and 100 Units/mL penicillin/streptomycin) at 37 °C in a humidified atmosphere of 5% CO_2. HaCaT cells were seeded at a density of 1×10^4 cells/mL in 96-well plates in 100 μL volume. After preincubation for 24 h, the cells were treated with **2** ranging from 40 to 1.25 μmol/L for an additional 24 h. Absorbance was measured at 450 nm using the microplate reader to determine cell viability, as described in the CCK-8 instructions.

4.14. Quantitative real-time polymerase chain reaction tests (qRT-PCR)

HaCaT cells were seeded at a density of 1×10^4 cells/mL in 6-well plates in 2 mL volume. After preincubation for 24 h in the humidified incubator at 37 °C and 5% CO_2, the cells were treated with 2.5 and 5 μmol/L of **2** for 24 h, followed by TNF-α (10 ng/mL) stimulation for another 24 h. RNA was isolated from HaCaT cells treated with **2** using a total RNA isolation reagent, followed by reverse transcription into cDNA using ABP 5 × All-in-One RT Master Mix. QRT-PCR was performed using Hieff® qPCR SYBR Green Master Mix (Low Rox Plus) (Cat. No. 11202ES08; Yeasen, Shanghai, China) and 0.2 mmol/L forward and reverse primers in a final volume of 10 μL. The reaction mixture was placed in ABI Quant Studio 5, and the resulting cDNA was amplified by incubating at 95 °C for 3 min, 40 cycles of denaturation at 95 °C for 10 s, annealing at 60 °C for 30 s, and extension at 72 °C for 30 s. Expression values were normalized to GAPDH.

4.15. Immunofluorescence analysis

Following treatment with **2**, the cell-seeded glass coverslips were fixed with 4% cold paraformaldehyde for 15 min, and 0.1% Triton X-100 was used for permeabilizing for 30 min. The coverslips were washed thrice with PBS to ensure no solution remained, and blocked with 3% BSA for 1 h. The cells were then incubated with a primary antibody specific to the NF-κB p65 subunit overnight at 4 °C, followed by a secondary antibody labeled with Alexa Fluor-594 for 1 h at room temperature in the dark. Subsequent staining with DAPI for 30 min at 37 °C was performed, followed by coverslip washing and sealing. Images were obtained using an OLYMPUS IX73 fluorescence microscope with excitation/emission wavelengths of 590 nm/617 nm for Alexa Fluor-594 and 360 nm/450 nm for DAPI.

4.16. Animal treatment

Babl/C mice at 7−8 weeks of age were randomly divided into four groups: blank control (vaseline, $n = 5$), positive control (tapinarof 1%, $n = 5$), **2** (2.0 mg/kg, $n = 5$), and IMQ groups ($n = 5$). Reagents were used as a single control across all groups. All mice were housed under standard conditions (temperature 25 ± 1 °C) with free access to a standard diet and water. After five days of adaptive feeding, mice were intraperitoneally injected with **2**. Tapinarof was dissolved to a mass volume concentration of 1% by 60% anhydrous ethanol and 40% glycerol and administered topically on the hair-free back, while **2** was administered by intraperitoneal injection for 7 days. Except for the blank control group, IMQ (62.5 mg/piece) was topically administered on the hair-free back of mice. Mouse weights and changes in back skins were observed and recorded daily before administration. After blood collection from the eyeballs, all the mice were euthanized, and part of their skin was preserved in 4% paraformaldehyde for 48 h. The remaining skin was frozen in a −80 °C refrigerator for further experiments.

4.17. Clinical severity score evaluation

The skin of mice was observed and photographed daily, and CSS was calculated daily based on erythema, scaling, and thickness on a scale of 0−4: 0, none; 1, mild; 2, moderate; 3, severe; and 4, very severe. The scoring was conducted daily for 7 days.

4.18. Histological analysis

Skin tissues immersed in 4% paraformaldehyde were dehydrated using gradient concentrations of ethanol, embedded in paraffin, and sectioned at a thickness of 5 μm. Paraffin sections of tissue were dewaxed with xylenes, rehydrated with an ethanol gradient, and stained with hematoxylin and eosin. The tissues were dehydrated in a gradient ethanol series and then vitrified with dimethylbenzene. The pathological changes were examined under a microscope.

4.19. Immunohistochemistry of Ki67 and IL-17

3% hydrogen peroxide solution was added into antigenically repaired paraffin sections to block endogenous peroxidase. After incubation sequentially with primary and secondary antibodies, sections were stained with DAB, and nuclei were restained. After color rendering, sections were dehydrated and prepared for microscopic examination under sealant.

4.20. Statistical analysis

All data were based on at least three independent experiments and interpreted as mean ± SD for each group. Comparisons between two groups were conducted using an unpaired, two-tailed Student's *t*-test. One-way or two-way ANOVA was used for multiple comparisons followed by the post hoc Bonferroni test. A *P*-value of <0.05 was considered statistically significant. All statistical analyses were performed using GraphPad Prism version 8.0 software (CA, USA).

Acknowledgments

This work was financially supported by the Program for Changjiang Scholars of Ministry of Education of the People's Republic of China (T2016088); the National Natural Science Foundation for Distinguished Young Scholars (81725021, China); the National Natural Science Foundation of China (Nos. 82003633, 32100321 and 32300335); the National Natural Science Foundation of Hubei Province (2023AFB791 and 2023AFB530, China); Knowledge Innovation Project of Wuhan Science and Technology Bureau (2023020201020534, China); the Research and Development Program of Hubei Province (2020BCA058, China); the Open Foundation of Hubei Key Laboratory of Wudang Local Chinese Medicine Research (WDCM2023010, China); Funded by Open Research Fund Program of State Key Laboratory of Biocatalysis and Enzyme Engineering (SKLBEE2023003, China); We thank the Experimental Animal Centre of Huazhong University of Science and Technology for assistance in the animal experimentation facilities and technical support.

Author contributions

This work was designed and guided by Yonghui Zhang and Changxing Qi, and the manuscript was revised by Changxing Qi and Weiguang Sun. Yulin Duan contributed to the extraction, isolation, identification, and manuscript preparation. Weiguang Sun and Yongqi Li contributed to the bioactivity tests. Zhengyi Shi and Yeting Zhang assisted in extraction and data analysis. Lanqin Li, Kun Huang and Zhiping Zhang assisted in the bioactive study.

Conflicts of interest

The authors declare no conflicts of interest.

Appendix A. Supporting information

Supporting data to this article can be found online at https://doi.org/10.1016/j.apsb.2024.02.002.

References

1. Griffiths CEM, Armstrong AW, Gudjonsson JE, Barker JNWN. Psoriasis. *Lancet* 2021;**397**:1301−15.
2. Michalek IM, Loring B, John SM. A systematic review of worldwide epidemiology of psoriasis. *J Eur Acad Dermatol Venereol* 2017;**31**:205−12.
3. Boehncke WH, Schon MP. Psoriasis. *Lancet* 2015;**386**:983−94.
4. Chandran V, Raychaudhuri SP. Geoepidemiology and environmental factors of psoriasis and psoriatic arthritis. *J Autoimmun* 2010;**34**:J314−21.
5. Lee HJ, Kim M. Challenges and future trends in the treatment of psoriasis. *Int J Mol Sci* 2023;**24**:13313−24.
6. Wu M, Dai C, Zeng F. Cellular mechanisms of psoriasis pathogenesis: a systemic review. *Clin Cosmet Invest Dermatol* 2023;**16**:2503−15.
7. Iwakura Y, Ishigame H. The IL-23/IL-17 axis in inflammation. *J Clin Invest* 2006;**116**:1218−22.
8. Gao W, Wang Z, Li W, Li Y, Liu M. Biomarkers and biologics related with psoriasis and psoriatic arthritis. *Int Immunopharm* 2023;**122**:110646−59.
9. Rendon A, Schakel K. Psoriasis pathogenesis and treatment. *Int J Mol Sci* 2019;**20**:1475−502.
10. Chedotal H, Narayanan D, Povlsen K, Gotfredsen CH, Brambilla R, Gajhede M, et al. Small-molecule modulators of tumor necrosis factor signaling. *Drug Discov Today* 2023;**28**:103575. 4.
11. Yang XW, Grossman RB, Xu G. Research progress of polycyclic polyprenylated acylphloroglucinols. *Chem Rev* 2018;**118**:3508−58.
12. Ciochina R, Grossman RB. Polycyclic polyprenylated acylphloroglucinols. *Chem Rev* 2006;**106**:3963−86.
13. Phang Y, Wang X, Lu Y, Fu W, Zheng C, Xu H. Bicyclic polyprenylated acylphloroglucinols and their derivatives: structural modification, structure−activity relationship, biological activity and mechanism of action. *Eur J Med Chem* 2020;**205**:112646−73.
14. Guttroff C, Baykal A, Wang H, Popella P, Kraus F, Biber N, et al. Polycyclic polyprenylated acylphloroglucinols: an emerging class of non-peptide-based MRSA- and VRE-active antibiotics. *Angew Chem Int Ed* 2017;**56**:15852−6.
15. Bridi H, Meirelles GC, von Poser GL. Structural diversity and biological activities of phloroglucinol derivatives from *Hypericum* species. *Phytochemistry* 2018;**155**:203−32.
16. Duan YL, Xie SS, Bu PF, Guo Y, Shi Z, Guo Y, et al. Hypaluton A, an immunosuppressive 3,4-*nor*-polycyclic polyprenylated acylphloroglucinol from *Hypericum patulum*. *J Org Chem* 2021;**86**:6478−85.
17. Duan YL, Deng YF, Bu PF, Xie S, Guo Y, Shi Z, et al. Discovery of *nor*-bicyclic polyprenylated acylphloroglucinols possessing diverse architectures with anti-hepatoma activities from *Hypericum patulum*. *Bioorg Chem* 2021;**111**:104902−12.
18. Guo Y, Huang F, Sun W, Zhou Y, Chen C, Qi C, et al. Unprecedented polycyclic polyprenylated acylphloroglucinols with anti-Alzheimer's activity from St. John's wort. *Chem Sci* 2021;**12**:11438−46.

19. Xie S, Tan X, Liu Y, Duan Y, Chen G, Feng H, et al. Hypersonins A−D, polycyclic polyprenylated acylphloroglucinols with a 1,2-*seco*-homoadamantane architecture from *Hypericum wilsonii*. *J Nat Prod* 2020;**83**:1804−9.
20. Lu W, Zhang Y, Li Y, Ye S, Luo J, Kong L, et al. Hyperbenzones A and B, two 1,2-*seco* and rearranged polycyclic polyprenylated acylphloroglucinols from *Hypericum beanii*. *Chin Chem Lett* 2022;**33**:4121−5.
21. Lou HY, Li YN, Yi P, Jian JY, Hu ZX, Gu W, et al. Hyperfols A and B: two highly modified polycyclic polyprenylated acylphloroglucinols from *Hypericum perforatum*. *Org Lett* 2020;**22**:6903−6.
22. Duan Y, Guo Y, Deng Y, Bu P, Shi Z, Cao Y, et al. Norprzewalsone A, a rearranged polycyclic polyprenylated acylphloroglucinol with a spiro[cyclopentane-1,3′-tricyclo[7.4.0.0^{1,6}]tridecane] core from *Hypericum przewalskii*. *J Org Chem* 2022;**87**:6824−31.
23. Cao J, Chen J, Du R, Zhang Q, Gan L, Zhang P, et al. Garcimultiflins A−C, unusual polycyclic polyprenylated acylphloroglucinols from the pericarps of *Garcinia multiflora* as interleukin-1β and pyroptosis inhibitors. *Org Chem Front* 2023;**10**:4311−9.
24. Zhang F, Yang J, Yi P, Li YN, Hao XJ, Yuan CM. Hyperpatone A, a polycyclic polyprenylated acylphloroglucinol with a rare 8/6/5/6/5 pentacyclic skeleton from *Hypericum patulum*. *Org Biomol Chem* 2023;**21**:140−6.
25. Li YW, Lu WJ, Zhou X, Zhang C, Li XY, Tang PF, et al. Diverse polycyclic polyprenylated acylphloroglucinols with anti-neuroinflammatory activity from *Hypericum beanii*. *Bioorg Chem* 2022;**127**:106005−16.
26. Lou HY, Ma FW, Yi P, Hu ZX, Gu W, Huang LJ, et al. Bioassay and UPLC−Q-Orbitrap−MS/MS guided isolation of polycyclic polyprenylated acylphloroglucinols from St. John's wort and their neuroprotective activity. *Arab J Chem* 2022;**15**:104057−68.
27. Wang AZ, Han H, Fang QQ, Tan CH. Structurally diverse polycyclic polyprenylated acylphloroglucinols with protective effect on human vein endothelial cells injured by high-glucose from *Hypericum acmosepalum* N. Robson. *Phytochemistry* 2023;**205**:113482−90.
28. Tanaka N, Kashiwada Y, Kim SY, Hashida W, Sekiya M, Ikeshiro Y, et al. Acylphloroglucinol, biyouyanagiol, biyouyanagin B, and related spirolactones from *Hypericum chinense*. *J Nat Prod* 2009;**72**:1447−52.
29. Zheng D, Chen Y, Wan S, Jiang J, Chen S, Zheng C, et al. Polycyclic polyprenylated acylphloroglucinol congeners from *Garcinia yunnanensis* Hu with inhibitory effect on α-hemolysin production in *Staphylococcus aureus*. *Bioorg Chem* 2021;**114**:105074−85.
30. Zeng YR, Yi P, Gu W, Xiao CX, Huang LJ, Tian DS, et al. Hypermonins A and B, two 6-norpolyprenylated acylphloroglucinols with unprecedented skeletons from *Hypericum monogynum*. *Org Biomol Chem* 2018;**16**:4195−8.
31. Xiang R, Hu L, Li S, Wei Z, Song Z, Chen Z, et al. Tiamulin inhibits TNF-α and alleviates psoriasis-like dermatitis. *J Dermatol Sci* 2022;**107**:32−40.
32. Guan JW, Xu Y, Yu W, Wei LH, Xue R, Yu H, et al. Biosensor-based active ingredient recognition system for screening TNF-α inhibitors from lotus leaves. *Anal Bioanal Chem* 2023;**415**:1641−55.
33. Wei W, Zeng Q, Wang Y, Guo X, Fan T, Li Y, et al. Discovery and identification of EIF2AK2 as a direct key target of berberine for anti-inflammatory effects. *Acta Pharm Sin B* 2023;**13**:2138−51.
34. Chen Y, Li K, Jiao M, Huang Y, Zhang Z, Xue L, et al. Reprogrammed siTNFα/neutrophil cytopharmaceuticals targeting inflamed joints for rheumatoid arthritis therapy. *Acta Pharm Sin B* 2023;**13**:787−803.
35. Chen L, Lv D, Wang S, Wang D, Chen X, Liu Y, et al. An SPR-based membrane protein-targeted active ingredients recognition strategy: construction and implementation in ligand screening from herbal medicines. *Anal Chem* 2020;**92**:3972−80.